Research Square

Preprints are preliminary reports that have not undergone peer review.
They should not be considered conclusive, used to inform clinical practice,
or referenced by the media as validated information.

Interfacial Particle Transport Driven by Negative Magnetophoretic Effects

HongWei Lin
Kunming University of Science and Technology
Feng Jiao
cfmf@kust.edu.cn

Kunming University of Science and Technology
Yongqing He
Southeast University

Research Article

Keywords: negative magnetophoresis, microfluidics, particle translocation, ferrofluid–water concentration boundary

Posted Date: November 27th, 2026

DOI: https://doi.org/10.21203/rs.3.rs-11808582/v1

License: This work is licensed under a Creative Commons Attribution 4.0 International License.
Read Full License

Additional Declarations: No competing interests reported.

Abstract

Negative magnetophoresis can displace diamagnetic particles in ferrofluids, but lateral deflection within a carrier stream does not establish transfer into an adjacent aqueous stream. Here, we investigate the size- and flow-rate-dependent translocation of 2, 5, and 10 μm polystyrene particles across the miscible concentration transition between co-flowing water-based ferrofluid and deionized water. A permanent magnet provides a transverse magnetic-field gradient, and microscopy-based trajectories and particle counts characterize migration and apparent crossing. We interpret the transport using a three-stage force-balance framework for migration in ferrofluid-rich liquid, passage through the concentration transition layer, and subsequent transport in water-rich liquid. The experimental transfer fraction of 2 μm particles decreases markedly with increasing flow rate, whereas the 5 μm fraction changes more modestly over the investigated range. In a separate flow-rate series, 10 μm particles exhibit approximately 94.69% translocation at 3 μL/min, followed by a substantial reduction at higher rates. Two-dimensional single-particle calculations support qualitative size- and residence-time trends but do not quantitatively predict measured transfer efficiencies. These findings characterize magnetically driven particle transport across a miscible co-flow boundary without establishing complete ferrofluid removal or biological compatibility.

1. Introduction

Continuous transfer of solid microparticles between adjacent microchannel streams requires more than transverse deflection within a single carrier liquid. Under laminar co-flow, the particles are advected downstream while lateral forces move them toward a neighbouring stream. Transfer can occur only if sufficient transverse displacement accumulates during the finite residence time available in the active region of the device. The position at which a particle appears to cross the stream boundary therefore influences its subsequent trajectory and potential collection, while particles that remain in the original carrier may still exhibit substantial lateral migration. Distinguishing deflection from interstream transfer is important for continuous particle handling and microfluidic medium-transfer strategies (Stone et al. 2004; Squires and Quake 2005; Whitesides 2006; Sackmann et al. 2014; Pamme 2007; Huang et al. 2004).

Negative magnetophoresis provides a label-free means of moving particles whose effective magnetic susceptibility is lower than that of the surrounding ferrofluid toward regions of weaker applied magnetic field (He et al. 2019; Suwa et al. 2023; Pamme 2006; Gijs et al. 2010; Rosensweig 1985; Hejazian and Nguyen 2015; Munaz et al. 2018). At low particle Reynolds number, the magnetic-force scale increases with particle volume, whereas Stokes drag is proportional to particle radius. Their balance therefore predicts a magnetophoretic slip velocity approximately proportional to the square of particle radius when the local susceptibility contrast, viscosity and magnetic-field gradient are fixed. This size dependence has been exploited to focus and separate nonmagnetic microparticles suspended in ferrofluids (Zhu et al. 2010; Zhu et al. 2011; Zeng et al. 2012; Zeng et al. 2013a; Zeng et al. 2013b; Hejazian and Nguyen 2016). Other work has investigated magnetic-field asymmetry, susceptibility contrast and configurations

involving multiple ferrofluid streams (Liang et al. 2013; Wilbanks et al. 2014; Zhu et al. 2014; Xue et al. 2020). Nevertheless, a stronger lateral magnetophoretic response does not, by itself, establish that a particle has passed from a ferrofluid-rich carrier into an adjacent water-rich stream.

Magnetic manipulation in continuous and co-flowing systems has substantial precedent. Free-flow magnetophoresis demonstrated field-driven deflection during downstream transport (Pamme et al. 2006). Zhou and Wang (2016) investigated microparticle focusing and separation using the boundary between co-flowing ferrofluid and a nonmagnetic liquid. Chen et al. (2017) combined negative magnetophoresis and inertial focusing for simultaneous particle separation and washing in ferrofluid–water co-flow, while related studies have coupled inertial separation or magnetic focusing with microchannel transport (Di Carlo 2009; Zhou et al. 2017; Chen et al. 2018). Accordingly, neither the use of adjacent ferrofluid and aqueous streams nor particle transfer toward an aqueous region is presented here as a first demonstration. The more specific question addressed in this work is how particle size and axial flow conditions influence the observed lateral trajectories, apparent boundary crossing and fraction of particles transferred in a miscible co-flow.

The physical nature of the boundary is important to that question. Because the carrier ferrofluid is water-based, it and the adjacent deionized-water stream are miscible. The optically apparent boundary therefore corresponds to a concentration transition rather than a sharp interface between immiscible liquids. Its spatial distribution can be influenced by streamwise advection, transverse nanoparticle diffusion and the magnetic response of the ferrofluid, consistent with established studies of transport and dispersion in laminar microflows (Kamholz et al. 1999; Kamholz and Yager 2001; Taylor 1953; Aris 1956; Stroock et al. 2002). Magnetic forcing may additionally redistribute ferrofluid constituents (Hejazian et al. 2016). As a solid particle approaches the transition region, the local effective magnetic susceptibility and viscosity may change with ferrofluid concentration, altering the balance between magnetic forcing and hydrodynamic resistance. Unlike transport across an immiscible liquid–liquid interface, for which interfacial tension and capillary effects may be relevant (Aubry and Singh 2008; Yin et al. 2018; Ruiz-Martín et al. 2022; Rigoni et al. 2022; Mondal et al. 2025), passage between these aqueous streams does not require a prescribed interfacial-tension barrier. The optical boundary is nevertheless not a direct measurement of the local nanoparticle concentration profile or transition-layer width.

Here, we investigate polystyrene microparticles with diameters of 2, 5 and 10 μm introduced in a ferrofluid-rich stream alongside deionized water in a straight microfluidic channel. A nearby permanent magnet generates a nonuniform field that drives transverse negative magnetophoresis toward the water-rich side. Microscopy-based observations and particle counts are used to examine size- and flow-rate-dependent migration and apparent translocation. To interpret the observations, we employ a quasi-two-dimensional, three-stage force-balance framework describing (i) lateral migration within the ferrofluid-rich stream, (ii) transport through the miscible concentration transition under spatially varying effective magnetic and viscous properties, and (iii) predominantly flow-driven motion after entry into the water-

rich region. The associated characteristic critical radius is defined for a specified migration distance and interaction time, rather than as a universal size threshold.

The experiments are complemented by idealized two-dimensional calculations that examine the dependence of representative particle trajectories on particle size and flow rate. These calculations identify geometric centerline crossing for individual model particles; that criterion is distinct from the experimental classification of transfer across the apparent concentration boundary and cannot directly predict population-level translocation efficiency. We therefore interpret agreement between the model and experimental trends qualitatively, through the competition among transverse magnetophoretic driving, viscous drag and downstream residence time. The intended contribution is a bounded mechanistic analysis of particle transport between miscible co-flowing media, rather than a new magnetic-force principle or a model of passage through an immiscible interface. The present evidence does not establish complete ferrofluid removal, biological compatibility or transport behaviour outside the investigated microparticle-size range.

2. Experimental section

The primary materials were a commercial water-based ferrofluid (EMG 705, Ferrotec Corp., Tokyo, Japan), deionized (DI) water, Tween 20 (Fisher Scientific Corp., Carlsbad, USA), and polystyrene microparticles (diameter 2 μm, 5 μm, 10 μm; Aladdin, China). The ferrofluid consisted of superparamagnetic Fe_3O_4 nanoparticles dispersed in an aqueous carrier liquid, with the following initial properties: volume fraction φ = 3.6%, magnetic susceptibility χ_f = 0.56, saturation magnetization M_{sat} = 16,560 A/m, dynamic viscosity $\eta_f = 1.6 \times 10^{-3}$ Pa·s, and density ρ_f = 1190 kg/m³. The Fe_3O_4 nanoparticles had an average diameter of 10 nm and a saturation magnetization of 4.6×10^5 A/m. The DI water had a density of 1000 kg/m³ and dynamic viscosity of 0.8937×10^{-3} Pa·s. The polystyrene microparticles had a diameter of 10 μm, solid content of 5%, and density of 1064 kg/m³.

The experimental setup included an inverted fluorescence microscope (Nikon TE2000U, Tokyo, Japan) integrated with a high-speed camera (PixeLINK-B742F, Ottawa, Canada) for visualization, a precision pipette (Eppendorf Research® plus, 0.5–10 μL range), precision syringe pumps (Harvard PHD 2000, Harvard Apparatus, USA) for controlled fluid delivery, syringes (Hamilton®, 1 mL volume, 4.61 mm inner diameter), and an ultrasonic cleaner (KX-1613T, Beijing Kexi Shiji Technology Co., Ltd., China) for sample dispersion.

The microfluidic chip was fabricated by standard soft lithography using polydimethylsiloxane (PDMS, Sylgard 184, Dow Corning, USA) as the substrate (Duffy et al. 1998; McDonald et al. 2000). As illustrated in Fig. 1(a), the chip design comprised two inlets and two outlets. The microchannel dimensions were length lc = 40 mm, width wc = 300 μm, and height hc = 100 μm. A rectangular N30-grade neodymium-iron-boron (NdFeB) permanent magnet was specified with nominal remanent magnetization Br = 1.08 T and dimensions of 25 mm in length (lm), 2 mm in width (wm), and 10 mm in height (hm). The magnet–channel edge separation was t = 3 mm. These dimensions describe the configuration investigated; they

are not claimed to have been obtained from an orthogonal-array, factorial, or other systematic design optimization. The magnetic-field sensitivity calculations at larger prescribed remanence values do not in themselves establish the field produced by a stacked-magnet assembly.

Figure 1 illustrates the channel geometry, magnet position, and experimental configuration. A ferrofluid-rich particle suspension and a water-rich receiving solution were introduced through separate inlets to form two parallel co-flowing streams. The permanent magnet was positioned adjacent to the ferrofluid-rich side of the channel and generated a non-uniform magnetic field primarily transverse to the main flow direction. Diamagnetic particles therefore migrated away from the high-field region and toward the water-rich stream by negative magnetophoresis. Depending on the balance between transverse migration and downstream advection, particles either remained in the ferrofluid-rich stream or passed through the concentration transition layer into the water-rich stream.

Key physical properties include the ferrofluid's initial volume fraction φ, magnetic susceptibility χ_f, saturation magnetization M_{sat}, dynamic viscosity η_f, and density ρ_f, as well as magnetic nanoparticles of average diameter d and saturation magnetization M_d. The aqueous phase is characterized by dynamic viscosity η_w and density ρ_w. Nonmagnetic particles possess radius R_p and density ρ_p. The microchannel dimensions are length l_c = 40 mm, width w_c = 300 μm, and height h_c = 100 μm. The permanent magnet has remanent magnetization Br (yielding a saturation magnetization of $M_s = Br/\mu_0$), with dimensions l_m, w_m, and h_m. The edge-to-edge distance between the microchannel and magnet is t, and the magnet center is located at horizontal distance x_m = 20 mm and vertical distance y_m from the channel entrance (coordinate origin at the center of the entrance cross-section).

3. Mechanical Model

Particle migration was modeled in the x–y midplane of the microchannel, where x denotes the streamwise direction and y the transverse direction from the ferrofluid stream toward the aqueous stream. Because the ferrofluid used in this study was water-based and co-flowed with deionized water, the boundary between the two streams is a miscible ferrofluid–water transition layer rather than a sharp immiscible liquid–liquid interface. Experimentally, this transition layer appears as a distinguishable interface due to laminar co-flow, slow transverse diffusion of magnetic nanoparticles, and magnetic confinement of the ferrofluid. Therefore, the term "interface" hereafter refers to the apparent concentration boundary between the ferrofluid-rich and water-rich regions.

Particle motion was approximated in the x–y channel midplane using a low-Reynolds-number force balance. The model assumes steady laminar co-flow, predominantly viscous particle motion, and magnetophoretic forcing calculated from an idealized permanent-magnet field. Gravity, buoyancy, out-of-plane migration, finite-size wall interactions, and feedback from the particle on the concentration distribution are not explicitly resolved. The ferrofluid–water boundary is treated as a miscible concentration transition layer, not a sharp interface between immiscible liquids; an interfacial-tension barrier or a persistent ferrofluid coating around each particle is therefore not imposed. The observation

windows are upstream of the outlets, so outlet-bath interactions are not included. These assumptions provide a simplified analytical framework (Happel and Brenner 1983), but they do not constitute independent experimental validation of the local field, transition-layer width, or complete three-dimensional particle trajectories.

Under the spatially non-uniform external magnetic field, diamagnetic particles suspended in the ferrofluid undergo negative magnetophoresis and traverse the ferrofluid–water concentration boundary through three coupled stages. In the lateral migration stage, the magnetic force $\mathbf{F_m}$ scales with particle volume ($\propto R_p^3$) while Stokes drag scales with radius ($\propto R_p$), yielding a net velocity $\propto R_p^2$ that favors larger particles. The interaction stage involves local modulation as particles enter the concentration gradient, where susceptibility χ and viscosity η decrease toward water values, reducing driving force. The final intrusion stage sees loss of magnetic contrast, with motion reverting to passive advection. This staged decomposition not only clarifies the physics but also enables predictive design of cutoff sizes via the derived critical radius expressions.

(1) Lateral Migration Stage

In a non-uniform magnetic field, a nonmagnetic particle experiences a magnetophoretic force arising from the field gradient and magnetization contrast (Zhu et al. 2011; Cao et al. 2020; Furlani 2006):

$$\varvec{F}_{\varvec{m}} = -\frac{4}{3}\pi R_p^3 \mu_0 \chi_f \nabla \varvec{H}^2$$

1

where μ_0 is the vacuum permeability ($4\pi \times 10^{-7}$ H/m), ∇ is the gradient operator, and H is the external magnetic field generated by the permanent magnet at the center of the particle. The complete analytical solutions for the *x* and *y* components of the magnetic field strength are (Zhu et al. 2011; Furlani 2006):

$$H_x(x,y) = \frac{M_s}{4\pi}\left\{\ln\left[\frac{((x-x_m)+0.5l_m)^2+((y+y_m)-0.5w_m)^2}{((x-x_m)+0.5l_m)^2+((y+y_m)+0.5w_m)^2}\right] - \ln\left[\frac{((x-x_m)-0.5l_m)^2+((y+y_m)-0.5w_m)^2}{((x-x_m)-0.5l_m)^2+((y+y_m)+0.5w_m)^2}\right]\right\}$$

2

$$H_y(x,y) = \frac{M_s}{2\pi}\left\{\tan^{-1}\left[\frac{w_m((x-x_m)+0.5l_m)}{((x-x_m)+0.5l_m)^2+(y+y_m)^2-0.25{w_m}^2}\right] - \tan^{-1}\left[\frac{w_m((x-x_m)-0.5l_m)}{((x-x_m)-0.5l_m)^2+(y+y_m)^2-0.25{w_m}^2}\right]\right\}$$

3

The field components in Eqs. (2) and (3) are analytical predictions calculated using the nominal magnet dimensions, position, and prescribed remanence; they are not magnetometer measurements. The particle-force curves obtained by inserting this field into Eq. (1) are likewise model-derived quantities. A quantitative field validation would require measurements of magnetic flux density at known positions along and across the microchannel, using a calibrated Hall probe or gaussmeter with the same magnet arrangement, orientation, and separation as the model. The resulting measured field profile should then be compared with the calculated profile on the same spatial coordinates. Such a quantitative field comparison is not included in the present data.

The hydrodynamic resistance caused by the viscosity of the surrounding medium hinders the movement of a single particle in ferrofluids. At low Reynolds number (*Re* < 1), the viscous resistance acting on the particle is (Happel and Brenner 1983):

$$\varvec{F}_{d} = 6\pi\eta_f R_p(\varvec{u}_{f} - \varvec{u}_{p})$$

4

where u_f and u_p are the velocity vectors of the ferrofluid and nonmagnetic particles, respectively. For a fully developed laminar flow, the fluid velocity in the microchannel cross-section can be expressed as (Zhu et al. 2011):

$$u_f = \frac{Q_f\pi}{2w_{cf}h_c} \times \left\{ \left[1 - \frac{2h_c}{\pi w_{cf}} \tanh\left(\frac{\pi w_{cf}}{2h_c} \right) \right] + \frac{1}{81} \left[1 - \frac{2h_c}{3\pi w_{cf}} \tanh\left(\frac{3\pi w_{cf}}{2h_c} \right) \right] \right\}^{-1} \times \left\{ \left[1 - \frac{\cosh\frac{\pi y}{h_c}}{\cosh\frac{\pi w_{cf}}{2h_c}} \right] \times \cos\frac{\pi z}{h_c} - \frac{1}{27} \left[1 - \frac{\cosh\frac{3\pi y}{h_c}}{\cosh\frac{3\pi w_{cf}}{2h_c}} \right] \times \cos\frac{3\pi z}{h_c} \right\}$$

5

where w_{cf} is the width of the ferrofluid stream in the microfluidic channel.

The trajectory of a nonmagnetic particle in a ferrofluid is governed by the magnetic force $\mathbf{F_m}$ induced by the magnetic field and the viscous drag $\mathbf{F_d}$ from the surrounding fluid. Neglecting inertial effects, the force balance for a single particle is expressed as:

$$\varvec{F}_{m} + \varvec{F}_{d} = 0$$

6

From Eqs. (1), (4), and (6), the velocity of nonmagnetic particles in the ferrofluid can be obtained as:

$$\varvec{u}_{\varvec{p}} = -\frac{2}{9}\frac{R_p^2 \mu_0 \chi_f}{\eta_f}\nabla \varvec{H}^2 + \varvec{u}_{\varvec{f}}$$

7

(2) Interaction stage

As particles approach the ferrofluid–water concentration transition layer, their motion is affected by local variations in ferrofluid concentration. Unlike an immiscible liquid–liquid interface, the present boundary is a miscible transition zone, avoiding the need for particles to overcome a discrete interfacial energy barrier (as in true liquid-liquid systems). Instead, its motion is governed by the local magnetic susceptibility (decreasing toward water values, thus reducing $|\mathbf{F_m}|$), viscosity (approaching that of water, lowering drag), magnetic-field gradient, and residence time within the transition layer. This continuous modulation enables smoother translocation than sharp-interface cases but introduces a tunable cutoff that depends on the layer thickness and flow residence time, as incorporated in the transition-layer critical radius $R_{c,t}$ (Eq. 14). The absence of a sharp barrier facilitates high efficiencies (> 95%) while preserving particle integrity.

Particle migration was again modeled in the *x*–*y* midplane (*x* streamwise, *y* transverse from ferrofluid-rich to water-rich stream). As both phases are aqueous, the apparent boundary is a finite ferrofluid–water concentration transition layer rather than a sharp immiscible interface. Under the low-Reynolds-number conditions of the device, particle inertia, gravity, buoyancy, and out-of-plane motion were neglected.

A diamagnetic particle suspended in a paramagnetic ferrofluid experiences a negative magnetophoretic force in a non-uniform magnetic field. Balancing this force with Stokes drag gives the transverse particle velocity in the ferrofluid-rich stream:

$$u_{p,y} = u_{f,y} + \frac{2R_p^2 \mu_0 \chi_f}{9\eta_f} G_y$$

8

$$G_y = -\frac{\partial H^2}{\partial y} > 0$$

9

where R_p is the particle radius, μ_0 is the vacuum permeability, χ_f and η_f are the magnetic susceptibility and dynamic viscosity of the ferrofluid-rich stream, respectively, and G_y represents the effective transverse magnetic-field-gradient term. Because the transverse fluid velocity is negligible in the present

co-flow configuration, the transverse magnetophoretic velocity scales as (from balancing $\mathbf{F_m} = (4/3)\pi R_p^3 \mu_0 \chi_f H \cdot \nabla H$ with Stokes drag $6\pi\eta_f R_p (u_p - u_f)$):

$$u_{p,y} \propto \frac{R_p^2 G_y}{\eta_f}.$$

10

Therefore, larger particles migrate more rapidly toward the water-rich stream than smaller particles.

The available migration time is determined primarily by the axial flow velocity. If a particle travels through an effective magnetic interaction length L_s with an average axial velocity $\bar{u}_{f,x}$, the residence time is approximately:

$$\tau_s \approx \int_{x_0}^{x_e} \frac{dx}{u_{f,x}} \approx \frac{L_s}{\bar{u}_{f,x}}$$

11

Using path-averaged values of the transverse magnetic-field-gradient term and axial flow velocity, the transverse displacement can be approximated as:

$$\Delta y_m(R_p) \approx \frac{2R_p^2 \mu_0 \chi_f}{9\eta_f} \frac{\bar{G}_y L_s}{\bar{u}_{f,x}}$$

12

A particle is transferred into the water-rich stream when its transverse displacement exceeds the required migration distance Δy_{req}. This gives the critical particle radius:

$$R_{c,t} = \left(\frac{9\bar{\eta}_t Q_f \delta_t}{2\mu_0 \bar{\chi}_t A_f \bar{G}_{y,t} L_t} \right)^{1/2}$$

13

Thus, particles with $R_p \geq R_c$ are expected to reach the water-rich stream, whereas smaller particles remain primarily in the ferrofluid-rich stream. Because $\bar{u}_{f,x}$ increases with flow rate and G_y increases with magnetic field strength, Eq. (13) predicts that increasing the flow rate raises the cutoff size, while increasing the magnetic field allows smaller particles to be transferred.

Within the ferrofluid–water concentration transition layer, the local susceptibility decreases and the local viscosity approaches that of water. These variations reduce the transverse magnetophoretic driving velocity during transfer. Their influence can be incorporated by defining an additional transition-layer

cutoff radius $R_{c,t}$, obtained using averaged transition-layer properties. The overall cutoff radius is therefore:

$$R_{c,\mathrm{overall}} = \max(R_c, R_{c,t})$$

14

The complete magnetic-field expressions, channel-flow solution, derivation of the critical radius, transition-layer formulation, and flow-rate separation window are provided in Supporting Information.

In addition, the dimensionless expression for the gradient of the squared magnetic field perpendicular to the flow can be abbreviated as (Zhu et al. 2011; Furlani 2006):

$$\frac{\partial \hat{H}^2}{\partial \hat{y}} = \backslash \mathrm{varvec} f\,(\hat{x}, \hat{y})$$

15

(3) Intrusion stage

Under the action of the negative magnetophoretic force, the particles traverse the interface formed between the ferrofluid and deionized water and migrate into the second phase (Zhou and Wang 2016; Chen et al. 2017). Once the particles enter the non-magnetic fluid, the difference in magnetization between the particles and the surrounding medium no longer exists (Rosensweig 1985; Zhu et al. 2011). Consequently, their subsequent motion is governed predominantly by the surrounding viscous flow field (Stone et al. 2004; Happel and Brenner 1983).

4. Results and Discussion

Under an external magnetic field, diamagnetic microparticles suspended in the ferrofluid undergo negative magnetophoresis and migrate away from the magnetic source. In the present co-flow microchannel, the permanent magnet serves two functions: it generates a transverse magnetic-field gradient to drive particle migration toward the water-rich stream and confines the ferrofluid-rich stream to stabilize the apparent ferrofluid–water concentration boundary. Therefore, particle transfer is jointly governed by the magnetic-field distribution, flow conditions, and residence time.

4.1 Magnetic-field-guided lateral migration toward the ferrofluid–water concentration boundary

Figure 2 presents calculated magnetic-field components and the corresponding model-derived magnetic-force components along the channel based on Eqs. (1)–(3), rather than directly measured magnetic-field maps. For the prescribed geometry, the calculated horizontal field component Hx changes sign about the nominal magnet center at x = 20 mm, whereas the calculated transverse component Hy

maintains its plotted sign. The predicted force components similarly indicate that transverse magnetic forcing can drive particles from the ferrofluid-rich toward the water-rich stream. The curves for larger remanence values are parametric calculations, not measurements of a specific stacked-magnet assembly. Figure 4 provides a qualitative visual comparison of co-flow with and without an applied magnet, but does not quantitatively validate the field magnitude or gradient.

Figure 6. Experimental images, reconstructed particle trajectories, and time-resolved motion of 10 μm polystyrene particles at three volumetric flow rates (Qf = 0.2, 0.6, and 1.0 μL/min). (a) Sequential experimental micrographs (top to bottom: 0.2, 0.6, and 1.0 μL/min). (b) Reconstructed transverse position versus axial position, with the legend ordered 0.2, 0.6, and 1.0 μL/min. (c) Axial displacement (blue curves, left axis) and instantaneous axial velocity (red curves, right axis). (d) Transverse displacement (blue curves, left axis) and instantaneous transverse velocity (red curves, right axis). In (c) and (d), the stacked rows are arranged from top to bottom as 0.2, 0.6, and 1.0 μL/min; velocities are estimated from successive tracked positions.

As shown in Fig. 6, panel (a) presents sequential experimental images of 10 μm particles, whereas panel (b) presents their reconstructed trajectories. The flow rates are ordered consistently as 0.2, 0.6, and 1.0 μL/min. Figures 6(c) and 6(d) present particle displacement (blue curves, left ordinate) and instantaneous velocity (red curves, right ordinate) in the x- and y-directions, respectively. In Fig. 6(c), the instantaneous axial velocity shows an overall decrease, which may reflect variations in the local magnetic force and viscous flow as particles move downstream. By contrast, the red transverse-velocity curve in Fig. 6(d), especially at the lowest flow rate, contains abrupt changes. After the particle enters the water-rich region, the magnetic susceptibility contrast with the surrounding liquid becomes small, so the negative magnetophoretic drive for further transverse migration is greatly reduced. The transverse displacement increment between successive frames can therefore be zero or too small to resolve. Because instantaneous transverse velocity is estimated from frame-to-frame displacement divided by the corresponding time interval, zero or unresolved increments interspersed with finite measured increments can appear as abrupt jumps in the red curve. Numerical differentiation of discrete tracked positions may accentuate these fluctuations (Crocker and Grier 1996; Sbalzarini and Koumoutsakos 2005). Thus, the fluctuations should not be interpreted as repeated physical accelerations of the particle in the transverse direction.

These results indicate that successful migration toward the ferrofluid–water concentration boundary requires coordinated control of magnetic-field strength, channel–magnet geometry, and flow rate. The magnetic field not only provides the transverse driving force ($\mathbf{F_{my}}$ dominant) but also stabilizes the concentration boundary via confinement of the ferrofluid-rich stream, suppressing diffusive broadening that would otherwise destabilize the interface (as seen in the *Br* = 0 T control). This dual role contrasts with previously studied hybrid inertial–magnetophoretic co-flow approaches (Chen et al. 2017; Zhou et al. 2017), where flow-induced lift assists transfer but may require higher velocities that reduce selectivity. Here, the low-flow regime (favoring magnetophoresis) enables residence times sufficient for near-complete translocation of larger particles while retaining smaller ones, achieving size-based

discrimination with minimal ferrofluid carryover. The flow rate determines the available residence time for particles to reach and pass through the transition layer, with the critical flow window balancing entry stability against migration time.

4.2 Size-dependent interfacial translocation behavior and translocation efficiency

After particles cross the ferrofluid–water concentration boundary and enter the nonmagnetic aqueous phase, the magnetic contrast between the particles and the surrounding medium becomes negligible. As a result, the negative magnetophoretic driving force is greatly reduced or effectively disappears. The subsequent particle motion is then governed mainly by the aqueous flow field, viscous drag, and wall effects (Brenner 1961; Goldman et al. 1967). A particle was classified as translocated only when its centroid completely crossed the ferrofluid–water concentration transition layer and entered the water-rich stream. Particles that remained within the ferrofluid-rich stream, approached the transition layer without crossing it, or only moved downstream were classified as non-translocated.

Figure 7 combines schematic trajectories with representative experimental micrographs to illustrate qualitative size-dependent behavior near the miscible ferrofluid–water concentration transition layer. The upper particle paths are schematic rather than experimental tracking overlays and cannot be used to determine quantitative crossing positions, migration velocities, or crossing frequencies. In the lower panels, the columns show 2 μm particles in Window 2, 5 μm particles in Window 3, and 10 μm particles in Window 2 (left to right); the rows correspond to Qf = 0.1, 1, and 2 μL/min (top to bottom). The expected size dependence is consistent with a magnetophoretic driving force that scales with particle volume and Stokes drag that scales with particle radius: under comparable local conditions, the transverse magnetophoretic slip velocity therefore increases approximately with the square of particle radius.

The schematic depicts distinctly different apparent crossing locations: 10 μm particles are illustrated crossing earlier, around Window 2, whereas 5 μm particles are illustrated crossing farther downstream, around Window 3. The 2 μm particles are represented by weaker transverse displacement and a less clearly localized crossing region. These paths illustrate the proposed size dependence but do not by themselves establish that a majority of a given particle population crossed within a particular window. Quantitative window-specific crossing fractions would require trajectory or particle-count data.

The schematic also illustrates the anticipated attenuation of transverse magnetic migration after entry into the water-rich stream, where the effective magnetic susceptibility of the surrounding liquid approaches that of water and the negative magnetophoretic driving force becomes small. Downstream motion is then expected to be dominated by viscous advection, with possible near-wall drag effects (Brenner 1961; Goldman et al. 1967). However, the schematic paths and still micrographs in Fig. 7 do not independently demonstrate post-crossing velocity relaxation, complete removal of ferrofluid constituents, or compatibility with downstream biological assays; these outcomes would require additional measurements.

Figure 8(d) examines 10 μm particles over a higher flow-rate range than the three-size comparison in Fig. 8(c). The efficiency was approximately 94.69% at Q = 3 μL/min but decreased strongly on increasing Q toward 6 μL/min. This observation is consistent with the reduced residence time available for transverse magnetic migration at larger axial flow rates, as anticipated by Eqs. (11)–(13). It does not, by itself, identify a unique critical flow rate or exclude additional influences of initial particle position, local flow conditions, and the concentration-transition width. These measurements on 10 μm particles should not be used to extrapolate the 5 μm efficiency to untested flow rates.

The efficiency in Fig. 8(c) is calculated directly from the observed translocated and non-translocated counts in Figs. 8(a) and 8(b), rather than obtained from an independent fitted curve. The red series represents 2 μm particles and shows a pronounced decline at the higher investigated flow rates. This behavior is physically consistent with competition between weak negative magnetophoretic transport and increasing axial advection: for otherwise similar local conditions, transverse magnetophoretic slip scales approximately with particle diameter squared (Eq. (10)), while the time available to accumulate transverse displacement decreases as axial flow increases (Eqs. (11)–(13)). Consequently, 2 μm particles are less likely to traverse the finite transition layer before leaving the effective magnetic interaction region as Q increases. In contrast, the 5 μm (green) series exhibits only a slight downward trend over the measured range, not complete insensitivity to flow rate. Their larger magnetophoretic mobility may provide sufficient displacement to maintain a high crossing fraction within that range despite the shorter residence time. These explanations are consistent with the force-balance model but are not a quantitative fit. Without verified independent replicate measurements and a documented uncertainty definition, the apparent differences are interpreted descriptively and no statistical significance is claimed.

The experimental trends can be compared qualitatively with the three-stage force-balance model. At fixed local magnetic-field gradient and medium properties, Eqs. (10)–(12) predict faster cross-stream magnetophoretic motion for larger particles and less accumulated transverse displacement as the mean axial flow speed increases. Accordingly, the stronger flow-rate sensitivity of 2 μm particles and the comparatively modest change of 5 μm efficiency over the tested range are consistent with the expected dependence on particle size and residence time. However, the present count-based efficiencies are not direct measurements of local magnetic force, concentration profiles, or the transverse displacement of an identical particle ensemble.

The model-derived critical radius should therefore be interpreted as a characteristic size for completing translocation within a prescribed observation length or residence time, rather than as an absolute threshold separating translocated and permanently retained particles. Particles below this characteristic size may still cross farther downstream, but their crossing locations are more sensitive to initial particle position, local flow conditions, and experimental resolution.

The present platform therefore provides size-dependent control of particle trajectories and crossing locations rather than a strict binary cutoff between translocated and retained particles.

4.3 Numerical particle-tracking results and experiment–model comparison

The existing analytical model offers a trend-level comparison with Figs. 7 and 8. Eq. (10) predicts a magnetophoretic slip-velocity scale proportional to dp^2 for fixed local field and fluid properties, whereas Eqs. (11) and (12) link accumulated displacement to the available residence time. Eq. (13) consequently predicts a larger characteristic crossing size as the axial speed increases. These relations agree in direction with the experimentally observed stronger flow-rate dependence of 2 μm translocation in Fig. 8(c), the slight decrease but relatively high 5 μm efficiency over the same measured range, and the fall in 10 μm efficiency at the higher rates shown separately in Fig. 8(d). The schematic paths in Fig. 7 are not quantitative tracks and are not used as numerical validation data.

To complement the analytical estimates, nine two-dimensional particle-tracking calculations were performed under the conditions described below. Their calculated centerline-crossing positions, crossing times, trajectory shapes, and magnetic-force magnitudes are presented in Table 1 and Figs. 9–10. These results provide a numerical description of size- and flow-rate-dependent particle transport under the specified model assumptions. The comparison with experiments remains at the level of physical trends: the simulated crossing criterion is the geometric channel centerline (y = 0), whereas the experimental translocation efficiency in Fig. 8 is based on particle counts entering the water-rich stream. Accordingly, the computed centerline-crossing results should not be interpreted as direct predictions of experimental translocation efficiency.

To complement the analytical model and the experimental observations, nine two-dimensional COMSOL particle-tracking cases were examined using particle diameters d_p = 2, 5, and 10 μm and equal inlet volumetric flow rates Q_{sim} = 0.3, 0.5, and 1.0 μL/min per inlet. The corresponding total flow rates were 0.6, 1.0, and 2.0 μL/min. Here Q_{sim} refers specifically to one numerical inlet and should not be conflated with the flow-rate notation used for individual experimental measurements. The computational channel was 40 mm long and 300 μm wide; its 100-μm depth was used for the conversion from volumetric flow rate to a two-dimensional inlet-velocity specification. Ferrofluid entered the lower branch and water entered the upper branch. In each case, one particle of density 1064 kg/m³ was released at (x_0, y_0) = (0.5 mm, − 85 μm). The N30 NdFeB magnet had dimensions 25 × 2 × 10 mm³, a remanence of 1.08 T, and a 3-mm edge-to-edge separation from the channel.

A bounded normalized ferrofluid-concentration field C(x,y) was regenerated for each flow rate on an 800 × 150 finite-volume grid. The reconstruction employed a conservative first-order upwind discretization following Patankar (1980) and a divergence-corrected interpolated flow field, with a diffusivity of 4.887 × 10^{-11} m²/s. Normalized concentration values of 1 and 0 were prescribed over the lower and upper inlet halves, respectively; sidewalls were treated as no-flux boundaries. Each reconstructed concentration table was imported into COMSOL as a spatially varying field and was held fixed during particle tracking.

The concentration was therefore flow-rate dependent but did not respond dynamically to the trajectory of an individual particle.

Table 1
Nine-condition simulation summary. Q is the flow rate per inlet; x_c and t_c denote first centerline crossing. Wall endpoints refer to first sampled upper-wall arrival; section endpoints are interpolated at x = 39 mm.

Particle diameter, D (μm)	Flow rate, Q_i (μL/min⁻¹)	x_{CL} (mm)	t_{CL} (s)	Termination condition	Tend (s)	Max |Fm| (pN)
10	1	2.20	1.27	Wall at 31.80 mm	28.40	19.480
10	0.5	1.45	1.51	Wall at 17.45 mm	46.85	16.083
10	0.3	1.06	1.64	Wall at 8.16 mm	26.80	14.752
5	1	4.51	2.92	x = 39 mm	31.00	4.272
5	0.5	3.29	4.05	Wall at 27.52 mm	56.40	2.937
5	0.3	2.51	4.93	Wall at 11.73 mm	43.60	2.372
2	1	9.96	6.87	x = 39 mm	24.98	0.610
2	0.5	7.15	9.75	x = 39 mm	58.42	0.446
2	0.3	5.95	13.24	Wall at 30.32 mm	87.15	0.327

The steady flow solution was recalculated after importing each concentration field, followed by transient particle tracking. Solutions were saved at 0.05-s intervals, with a maximum internal time step of 0.005 s. The integrated inlet rates differed from their nominal values by approximately 0.39%, while downstream channel-section fluxes were close to twice the prescribed per-inlet rate. The first geometric centerline crossing was defined as the earliest time at which the particle centroid attained y = 0; its position x_{CL} and elapsed time t_{CL} were obtained by linear interpolation between stored points. Each tracked trajectory was retained only until the centroid reached the x = 39 mm observation plane or the imposed upper-wall termination level y = 150 μm. The latter is a point-particle termination rule, not a finite-radius contact or adhesion calculation. Because y = 0 is a geometric line rather than a defined concentration isosurface, centerline crossing must not be equated with complete passage through the ferrofluid–water transition layer or successful outlet recovery.

To interpret the size- and flow-dependent migration trends observed experimentally in Figs. 6–8, the nine simulations were compared using a common particle-release location and a consistent geometric

centerline-crossing criterion. The calculations are supplementary mechanistic comparisons rather than a numerical reproduction of the experimental translocation-efficiency measurements.

At Q_{sim} = 1.0 µL/min per inlet, particles with diameters of 10, 5, and 2 µm first reached the channel centerline at x_{CL} = 2.20, 4.51, and 9.96 mm, respectively, after t_{CL} = 1.27, 2.92, and 6.87 s (Table 1). The corresponding trajectories in Fig. 9 show that larger particles acquire a greater transverse displacement over the same downstream distance. At a fixed location in the prescribed force model, magnetic force scales with particle diameter cubed, whereas the Stokes drag coefficient scales linearly with diameter. The resulting magnetophoretic slip therefore scales approximately as d^2 when the local concentration, field, and viscosity are unchanged. This scaling explains the upstream shift for larger particles but does not imply that peak forces sampled along different trajectories must follow a strict d^3 ratio.

For a fixed particle size, decreasing Q_{sim} from 1.0 to 0.3 µL/min moved the centerline-crossing location upstream: from 2.20 to 1.06 mm for 10-µm particles, from 4.51 to 2.51 mm for 5-µm particles, and from 9.96 to 5.95 mm for 2-µm particles. In contrast, the elapsed times to first centerline crossing increased from 1.27 to 1.64 s, from 2.92 to 4.93 s, and from 6.87 to 13.24 s, respectively. Thus, an upstream crossing position does not mean a shorter crossing time. Lower axial advection allows more transverse displacement per unit downstream distance even though particles may take longer to reach the geometric centerline.

The peak magnetic-force magnitudes in the 10-µm cases were 19.480, 16.083, and 14.752 pN at Q_{sim} = 1.0, 0.5, and 0.3 µL/min, respectively (Fig. 10 and Table 1). The corresponding maxima were 4.272, 2.937, and 2.372 pN for 5 µm, and 0.610, 0.446, and 0.327 pN for 2 µm. Strong upstream peaks occurred where the prescribed field and concentration-dependent force sampled along the trajectories were greatest; smaller downstream features were also visible in some cases. Their detailed origin cannot be established from force magnitude alone without examining the simultaneous local concentration and magnetic-field gradient.

Six of the nine simulated trajectories reached the imposed upper-wall termination level before the x = 39 mm observation plane: all three 10-µm cases, the 5-µm cases at Q_{sim} = 0.5 and 0.3 µL/min, and the 2-µm case at Q_{sim} = 0.3 µL/min. For 10-µm particles, decreasing Q_{sim} from 1.0 to 0.3 µL/min moved the wall-termination location from 31.80 to 8.16 mm. Only the 5-µm case at Q_{sim} = 1.0 µL/min and the 2-µm cases at Q_{sim} = 1.0 and 0.5 µL/min reached x = 39 mm without meeting that termination condition.

At x = 39 mm, the three non-wall-terminated trajectories had transverse centroid positions of approximately 112.69, 51.68, and 108.37 µm, respectively. The reported local normalized concentrations at those endpoints were 0.027, 0.153, and 0.121. These values refer to the modeled concentration field at the particle positions and do not quantify the nanoparticle concentration or purity of a collected outlet fraction. Further, the numerical wall condition does not resolve a finite particle's contact with the wall. These nine single-release cases cannot independently predict the experimental translocation

efficiencies, which require a population of initial positions and a concentration- or outlet-based transfer criterion.

5. Conclusions

This study demonstrates a label-free microfluidic strategy for controlling the translocation of diamagnetic microparticles from a ferrofluid-rich stream into an aqueous stream by coupling negative magnetophoresis with crossing of a miscible ferrofluid–water concentration transition layer. Rather than introducing a new negative magnetophoretic separation principle, this work focuses on elucidating the transport mechanism associated with particle migration across a finite concentration boundary. The external permanent magnet generates a transverse magnetic-field gradient that drives particle migration away from the ferrofluid-rich region while simultaneously stabilizing the co-flow concentration boundary through magnetic confinement.

Particle transport across the ferrofluid–water concentration transition layer was represented by a three-stage framework: (i) lateral magnetophoretic migration in the ferrofluid-rich stream, (ii) traversal of a region with varying effective magnetic and viscous properties, and (iii) predominantly hydrodynamic motion after entry into the water-rich stream. The analytical force-balance model predicts stronger transverse migration for larger diamagnetic particles and less available crossing time at higher axial flow rates. The nine-condition numerical particle-tracking analysis further quantifies first geometric centerline-crossing positions and times and the magnetic-force magnitudes along simulated trajectories. The size- and flow-rate-dependent trends are qualitatively consistent with the experimental observations.

Experiments with 2, 5, and 10 μm polystyrene particles illustrate the competition between particle size, magnetic forcing, and available residence time. The 2 μm efficiency decreases markedly at higher flow rates in the tested range, whereas the 5 μm efficiency decreases only slightly; a separate 10 μm series shows a strong decrease at still higher flow rates. The characteristic critical radius from the model should be interpreted as a design-scale prediction for a specified channel length and interaction time, not as an experimentally established absolute size cutoff.

Although the numerical calculations are reported for the specified model conditions, their geometric centerline-crossing results are not equivalent to experimentally measured transfer across the full miscible concentration transition layer or to outlet recovery. A direct quantitative validation of translocation efficiency would require matched initial particle distributions, an experimentally characterized concentration-transition profile, and the same crossing definition in simulations and experiments. The current model–experiment comparison therefore supports mechanistic interpretation without claiming a quantitative prediction of population-level separation efficiency.

Overall, this work provides a mechanistic understanding of size-dependent particle transport across a miscible ferrofluid–water concentration transition layer and establishes design principles for controlling particle trajectories and crossing locations in negative-magnetophoretic co-flow systems. The present

study is limited to micrometer-sized polystyrene particles and relatively low-throughput operating conditions. Future studies should quantify ferrofluid nanoparticle carryover after translocation, evaluate performance using mixed-particle samples and complex biological matrices, and further investigate three-dimensional effects and device scaling. In addition, biological validation will be required to assess ferrofluid exposure effects, including nanoparticle compatibility and potential impacts on cells or other biological particles. Optimization of magnetic-field configuration, channel geometry, and parallelized device architectures may further improve throughput and expand the applicability of this strategy toward more complex sample-processing applications.

Declarations

Author Contribution

Hongwei Lin conducted the experiments and numerical simulations, prepared the figures, and wrote the original draft of the manuscript. Feng Jiao and Yongqing He provided academic guidance and scientific advice throughout the study. All authors reviewed the entire manuscript.

Acknowledgments

The authors gratefully acknowledge financial support from the Yunnan Fundamental Research Projects (Grants No. 202401AT070348 and 202501AT070325) and the National Natural Science Foundation of China (Grant No. 52366005). We also acknowledge support from Yunnan Province's high-level talent program and unique support plan.

Data availability

The data supporting this study's findings are available from the corresponding author upon reasonable request.

References

1. Aris R (1956) On the dispersion of a solute in a fluid flowing through a tube. Proc R Soc Lond A 235:67–77. https://doi.org/10.1098/rspa.1956.0065
2. Aubry N, Singh P (2008) Physics underlying controlled self-assembly of micro- and nanoparticles at a two-fluid interface using an electric field. Phys Rev E 77:056302. https://doi.org/10.1103/PhysRevE.77.056302
3. Brenner H (1961) The slow motion of a sphere through a viscous fluid towards a plane surface. Chem Eng Sci 16:242–251. https://doi.org/10.1016/0009-2509(61)80035-3

4. Cao Q, Fan Q, Chen Q, Liu C, Han X, Li L (2020) Recent advances in manipulation of micro- and nano-objects with magnetic fields at small scales. Mater Horiz 7:638–666. https://doi.org/10.1039/C9MH00714H
5. Chen Q, Li D, Lin J, Wang M, Xuan X (2017) Simultaneous separation and washing of nonmagnetic particles in an inertial ferrofluid/water coflow. Anal Chem 89:6915–6920. https://doi.org/10.1021/acs.analchem.7b01608
6. Chen Q, Li D, Malekanfard A, Cao Q, Lin J, Wang M, Han X, Xuan X (2018) Tunable, sheathless focusing of diamagnetic particles in ferrofluid microflows with a single set of overhead permanent magnets. Anal Chem 90:8600–8606. https://doi.org/10.1021/acs.analchem.8b01813
7. Crocker JC, Grier DG (1996) Methods of digital video microscopy for colloidal studies. J Colloid Interface Sci 179:298–310. https://doi.org/10.1006/jcis.1996.0217
8. Di Carlo D (2009) Inertial microfluidics. Lab Chip 9:3038–3046. https://doi.org/10.1039/B912547G
9. Duffy DC, McDonald JC, Schueller OJA, Whitesides GM (1998) Rapid prototyping of microfluidic systems in poly(dimethylsiloxane). Anal Chem 70:4974–4984. https://doi.org/10.1021/ac980656z
10. Furlani EP (2006) Analysis of particle transport in a magnetophoretic microsystem. J Appl Phys 99:024912. https://doi.org/10.1063/1.2164531
11. Gijs MAM, Lacharme F, Lehmann U (2010) Microfluidic applications of magnetic particles for biological analysis and catalysis. Chem Rev 110:1518–1563. https://doi.org/10.1021/cr9001929
12. Goldman AJ, Cox RG, Brenner H (1967) Slow viscous motion of a sphere parallel to a plane wall—I. Motion through a quiescent fluid. Chem Eng Sci 22:637–651. https://doi.org/10.1016/0009-2509(67)80047-2
13. Happel J, Brenner H (1983) Low Reynolds number hydrodynamics: with special applications to particulate media. Martinus Nijhoff, The Hague. https://doi.org/10.1007/978-94-009-8352-6
14. He Y, Luo L, Huang S (2019) Magnetic manipulation on the unlabeled nonmagnetic particles. Int J Mod Phys B 33:1950047. https://doi.org/10.1142/S0217979219500474
15. Hejazian M, Nguyen NT (2015) Negative magnetophoresis in diluted ferrofluid flow. Lab Chip 15:2998–3005. https://doi.org/10.1039/C5LC00427F
16. Hejazian M, Nguyen NT (2016) Magnetofluidic concentration and separation of non-magnetic particles using two magnet arrays. Biomicrofluidics 10:044103. https://doi.org/10.1063/1.4955421
17. Hejazian M, Phan DT, Nguyen NT (2016) Mass transport improvement in microscale using diluted ferrofluid and a non-uniform magnetic field. RSC Adv 6:62439–62444. https://doi.org/10.1039/C6RA11703A
18. Huang LR, Cox EC, Austin RH, Sturm JC (2004) Continuous particle separation through deterministic lateral displacement. Science 304:987–990. https://doi.org/10.1126/science.1094567
19. Kamholz AE, Weigl BH, Finlayson BA, Yager P (1999) Quantitative analysis of molecular interaction in a microfluidic channel: the T-sensor. Anal Chem 71:5340–5347. https://doi.org/10.1021/ac990504j

20. Kamholz AE, Yager P (2001) Theoretical analysis of molecular diffusion in pressure-driven laminar flow in microfluidic channels. Biophys J 80:155–160. https://doi.org/10.1016/S0006-3495(01)76003-1
21. Liang L, Zhang C, Xuan X (2013) Enhanced separation of magnetic and diamagnetic particles in a dilute ferrofluid. Appl Phys Lett 102:234101. https://doi.org/10.1063/1.4810874
22. McDonald JC, Duffy DC, Anderson JR, Chiu DT, Wu H, Schueller OJA, Whitesides GM (2000) Fabrication of microfluidic systems in poly(dimethylsiloxane). Electrophoresis 21(2000010121:127):27–40. https://doi.org/10.1002/(SICI)1522-2683. ::AID-ELPS27>3.0.CO;2-C
23. Mondal S, Abbasi N, Tsai SSH, Griffiths IM (2025) Migration of magnetic microparticles through a liquid–liquid interface under an external magnetic field. Phys Fluids 37:022010. https://doi.org/10.1063/5.0250330
24. Munaz A, Shiddiky MJA, Nguyen NT (2018) Magnetophoretic separation of diamagnetic particles through parallel ferrofluid streams. Sens Actuators B Chem 275:459–469. https://doi.org/10.1016/j.snb.2018.07.176
25. Pamme N (2006) Magnetism and microfluidics. Lab Chip 6:24–38. https://doi.org/10.1039/B513005K
26. Pamme N (2007) Continuous flow separations in microfluidic devices. Lab Chip 7:1644–1659. https://doi.org/10.1039/B712784G
27. Pamme N, Eijkel JCT, Manz A (2006) On-chip free-flow magnetophoresis: separation and detection of mixtures of magnetic particles in continuous flow. J Magn Magn Mater 307:237–244. https://doi.org/10.1016/j.jmmm.2006.04.008
28. Patankar SV (1980) Numerical heat transfer and fluid flow. Hemisphere Publishing Corporation, New York
29. Rigoni C, Beaune G, Harnist B, Sohrabi F, Timonen JVI (2022) Ferrofluidic aqueous two-phase system with ultralow interfacial tension and micro-pattern formation. Commun Mater 3:26. https://doi.org/10.1038/s43246-022-00249-z
30. Rosensweig RE (1985) Ferrohydrodynamics. Cambridge University Press, Cambridge
31. Ruiz-Martín D, Rivero-Rodriguez J, Sánchez-Sanz M (2022) Solid particles moving parallel to a deformable liquid–liquid interface in a micro-channel: migration forces. J Fluid Mech 948:A44. https://doi.org/10.1017/jfm.2022.683
32. Sackmann EK, Fulton AL, Beebe DJ (2014) The present and future role of microfluidics in biomedical research. Nature 507:181–189. https://doi.org/10.1038/nature13118
33. Sbalzarini IF, Koumoutsakos P (2005) Feature point tracking and trajectory analysis for video imaging in cell biology. J Struct Biol 151:182–195. https://doi.org/10.1016/j.jsb.2005.06.002
34. Squires TM, Quake SR (2005) Microfluidics: fluid physics at the nanoliter scale. Rev Mod Phys 77:977–1026. https://doi.org/10.1103/RevModPhys.77.977

35. Stone HA, Stroock AD, Ajdari A (2004) Engineering flows in small devices: microfluidics toward a lab-on-a-chip. Annu Rev Fluid Mech 36:381–411. https://doi.org/10.1146/annurev.fluid.36.050802.122124
36. Stroock AD, Dertinger SKW, Ajdari A, Mezić I, Stone HA, Whitesides GM (2002) Chaotic mixer for microchannels. Science 295:647–651. https://doi.org/10.1126/science.1066238
37. Suwa M, Tsukahara S, Watarai H (2023) Applications of magnetic and electromagnetic forces in micro-analytical systems. Lab Chip 23:1097–1127. https://doi.org/10.1039/D2LC00702A
38. Taylor GI (1953) Dispersion of soluble matter in solvent flowing slowly through a tube. Proc R Soc Lond A 219:186–203. https://doi.org/10.1098/rspa.1953.0139
39. Whitesides GM (2006) The origins and the future of microfluidics. Nature 442:368–373. https://doi.org/10.1038/nature05058
40. Wilbanks JJ, Kiessling G, Zeng J, Zhang C, Tzeng TR, Xuan X (2014) Exploiting magnetic asymmetry to concentrate diamagnetic particles in ferrofluid microflows. J Appl Phys 115:044907. https://doi.org/10.1063/1.4862965
41. Xue CD, Sun ZP, Li YJ, Chen JF, Liu B, Qin KR (2020) Separation of micro and sub-micro diamagnetic particles in dual ferrofluid streams based on negative magnetophoresis. Electrophoresis 41:909–916. https://doi.org/10.1002/elps.202000002
42. Yin T, Shin D, Frechette J, Colosqui CE, Drazer G (2018) Dynamic effects on the mobilization of a deposited nanoparticle by a moving liquid–liquid interface. Phys Rev Lett 121:238002. https://doi.org/10.1103/PhysRevLett.121.238002
43. Zeng J, Chen C, Vedantam P, Brown V, Tzeng TRJ, Xuan X (2012) Three-dimensional magnetic focusing of particles and cells in ferrofluid flow through a straight microchannel. J Micromech Microeng 22:105018. https://doi.org/10.1088/0960-1317/22/10/105018
44. Zeng J, Chen C, Vedantam P, Tzeng TR, Xuan X (2013a) Magnetic concentration of particles and cells in ferrofluid flow through a straight microchannel using attracting magnets. Microfluid Nanofluid 15:49–55. https://doi.org/10.1007/s10404-012-1126-0
45. Zeng J, Deng Y, Vedantam P, Tzeng TR, Xuan X (2013b) Magnetic separation of particles and cells in ferrofluid flow through a straight microchannel using two offset magnets. J Magn Magn Mater 346:118–123. https://doi.org/10.1016/j.jmmm.2013.07.021
46. Zhou R, Wang C (2016) Multiphase ferrofluid flows for micro-particle focusing and separation. Biomicrofluidics 10:034101. https://doi.org/10.1063/1.4948656
47. Zhou Y, Song L, Yu L, Xuan X (2017) Inertially focused diamagnetic particle separation in ferrofluids. Microfluid Nanofluid 21:14. https://doi.org/10.1007/s10404-016-1839-6
48. Zhu T, Marrero F, Mao L (2010) Continuous separation of non-magnetic particles through negative magnetophoresis inside ferrofluids. In: Proceedings of the 5th IEEE International Conference on Nano/Micro Engineered and Molecular Systems, pp 1006–1011. https://doi.org/10.1109/NEMS.2010.5592591

49. Zhu T, Lichlyter DJ, Haidekker MA, Mao L (2011) Analytical model of microfluidic transport of non-magnetic particles in ferrofluids under the influence of a permanent magnet. Microfluid Nanofluid 10:1233–1245. https://doi.org/10.1007/s10404-010-0754-5
50. Zhu T, Cheng R, Liu Y, He J, Mao L (2014) Combining positive and negative magnetophoreses to separate particles of different magnetic properties. Microfluid Nanofluid 17:973–982. https://doi.org/10.1007/s10404-014-1396-9

Figures

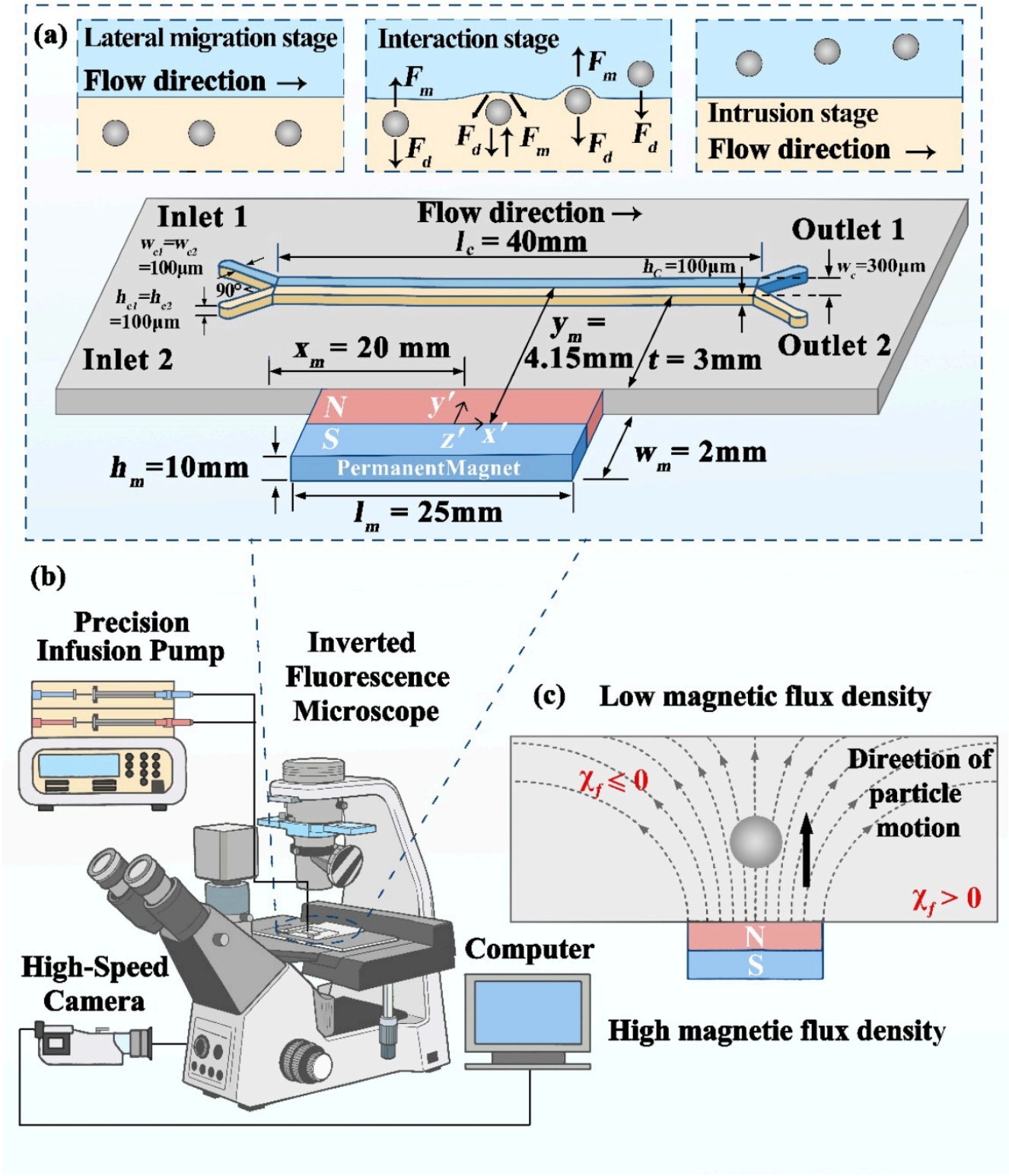


Figure 1

Microfluidic device and experimental configuration. (a) Geometry and relative positions of the microchannel and permanent magnet. (b) Experimental setup for fluid delivery and particle imaging. A ferrofluid-rich particle suspension and deionized water were introduced through separate inlets to form parallel co-flowing streams. (c) Schematic of negative magnetophoresis, in which a diamagnetic

particle suspended in a magnetically susceptible medium migrates toward a region of lower magnetic-field strength.

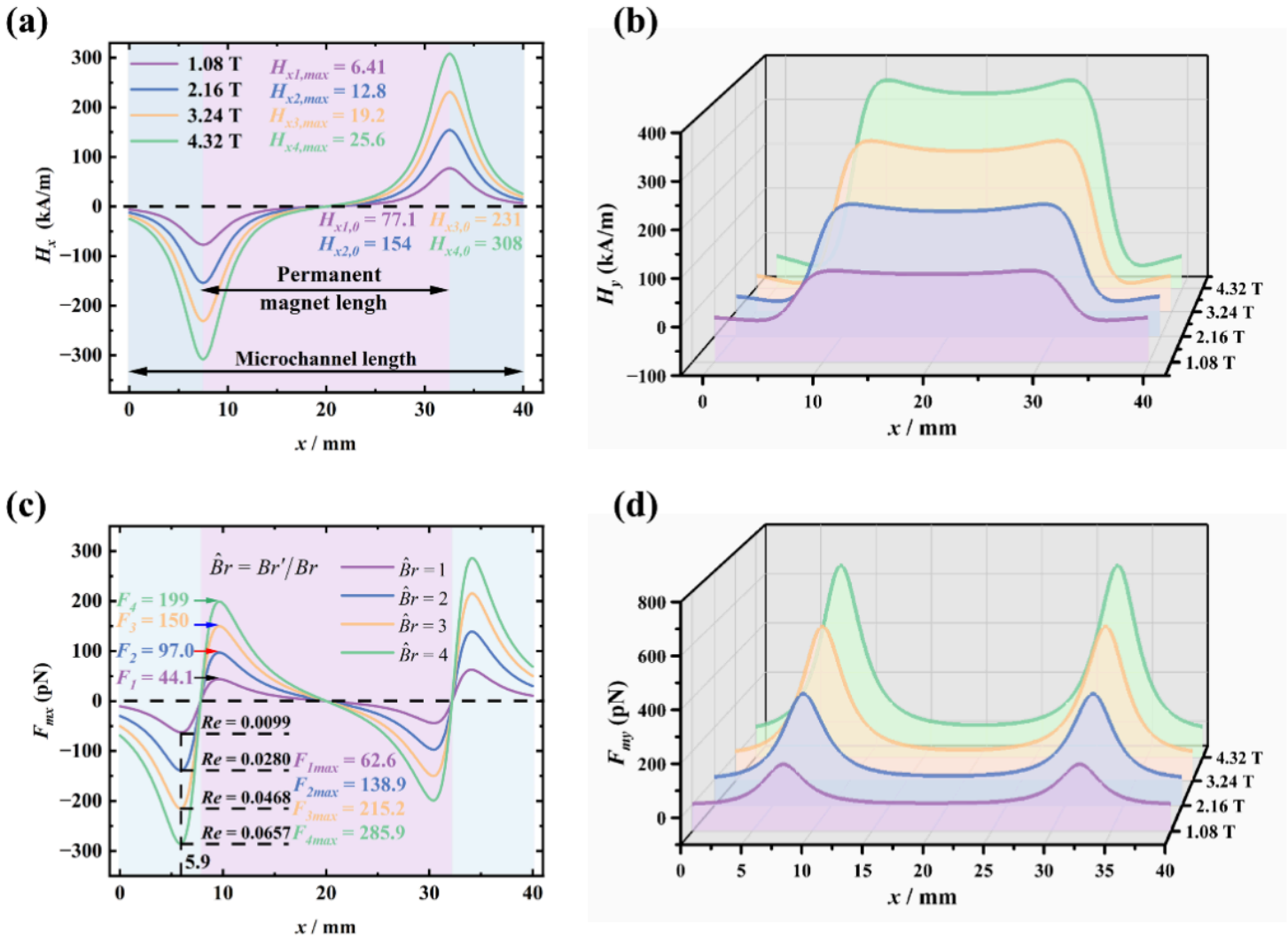


Figure 2

Analytical calculations of magnetic-field components and model-derived magnetic-force components along the microchannel for prescribed remanence inputs. (a) Axial magnetic-field strength Hx. (b) Transverse magnetic-field strength Hy. (c) Axial magnetic force Fmx. (d) Transverse magnetic force Fmy. The plotted values are calculations based on the nominal cuboid-magnet geometry and particle-force model, not direct magnetic-field or force measurements; higher remanence inputs are parameter variations and are not verified stacked-magnet measurements.

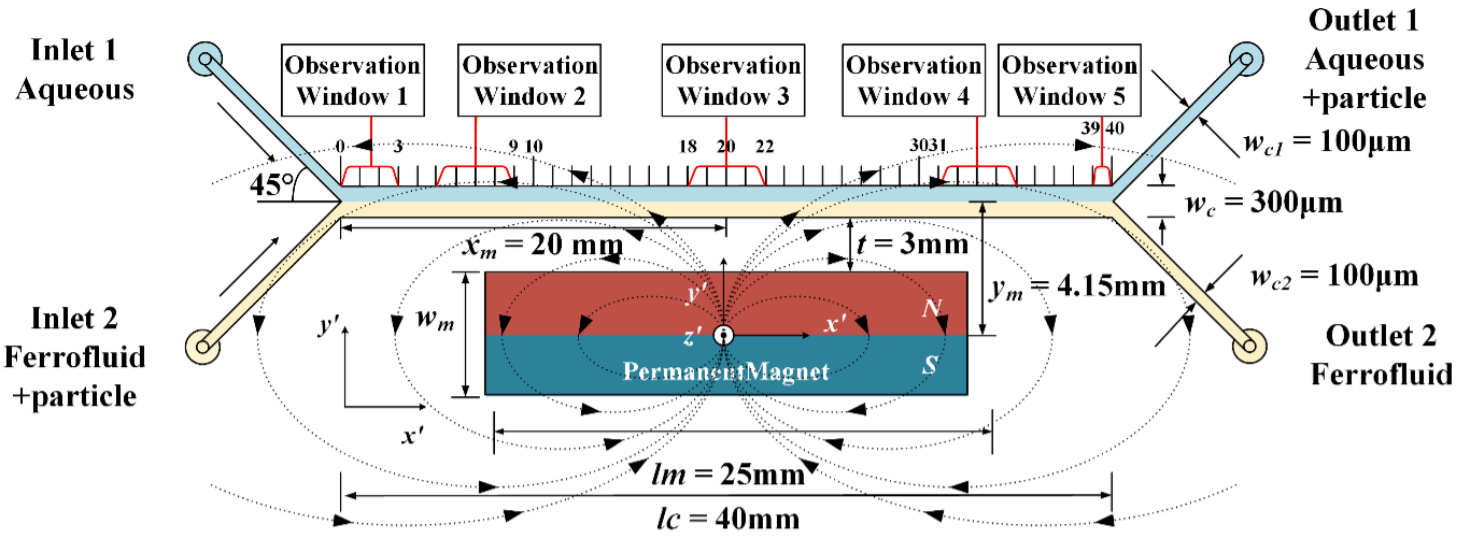


Figure 3

Coordinate system, magnet position, and locations of the particle-observation windows along the microchannel.

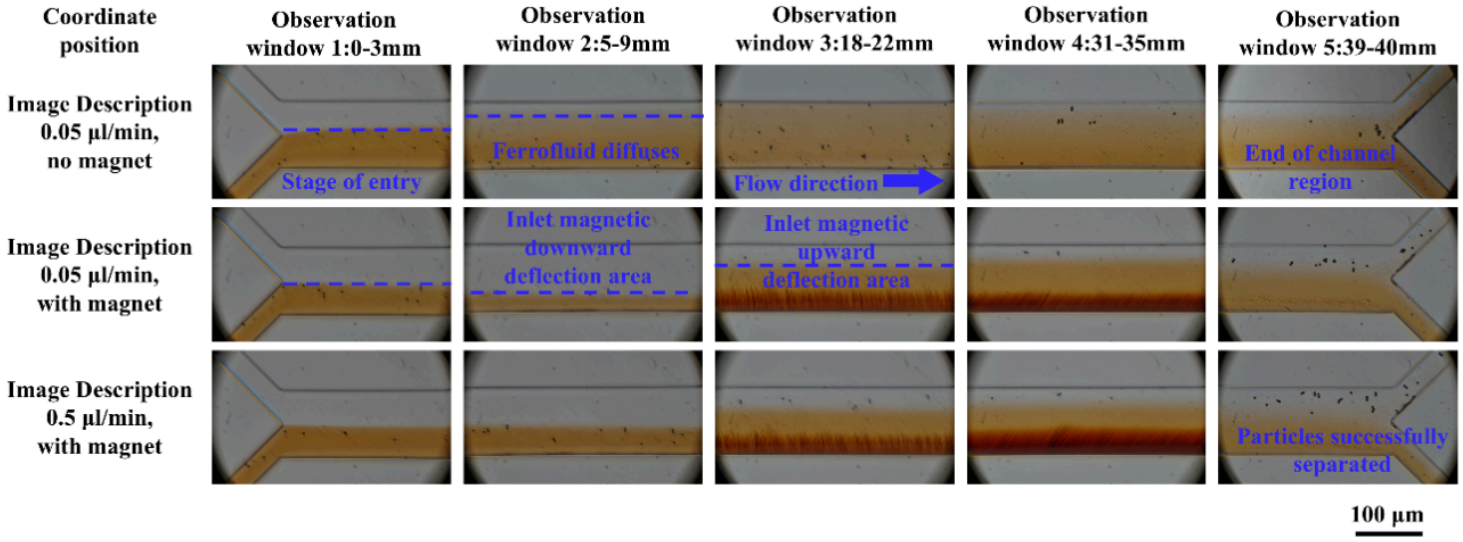


Figure 4

Particle motion within the microchannel under different magnetic-field conditions and flow velocities. The magnetic-field-free condition is *Br* = 0 T, and the magnetic-field condition is *Br* = 1.08 T.

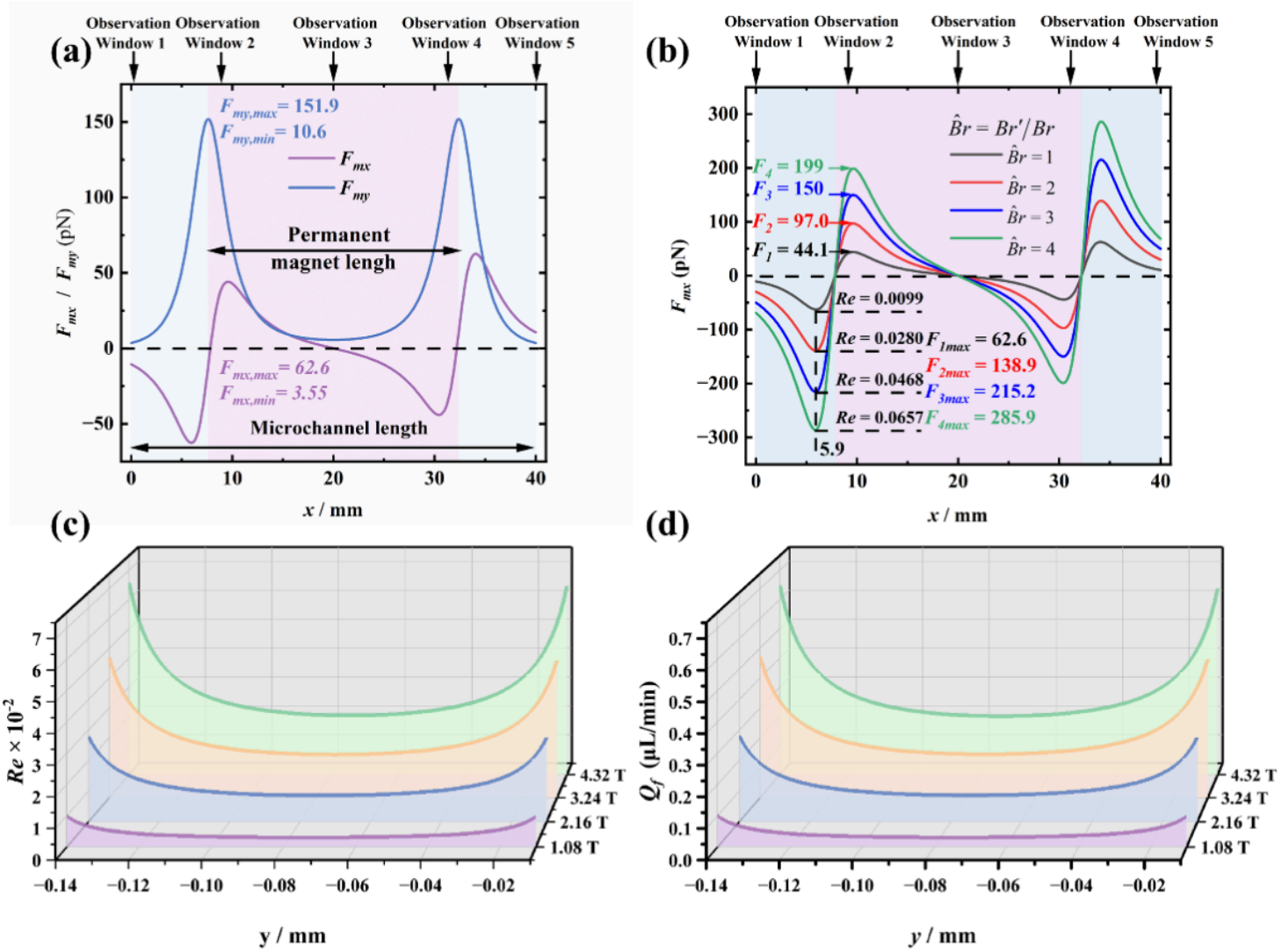


Figure 5

Model-calculated magnetic-force distribution and derived critical flow conditions for prescribed magnetic input parameters. (a) Axial magnetic-force component along the channel. (b) Calculated axial critical flow-field quantity. (c) Calculated transverse critical flow-field quantity. (d) Calculated critical volumetric flow rate. Br denotes the reference nominal remanence and Br' denotes the prescribed remanence used in the parametric curves. These are analytical/model-based outputs, not measured field profiles or independently validated numerical results.

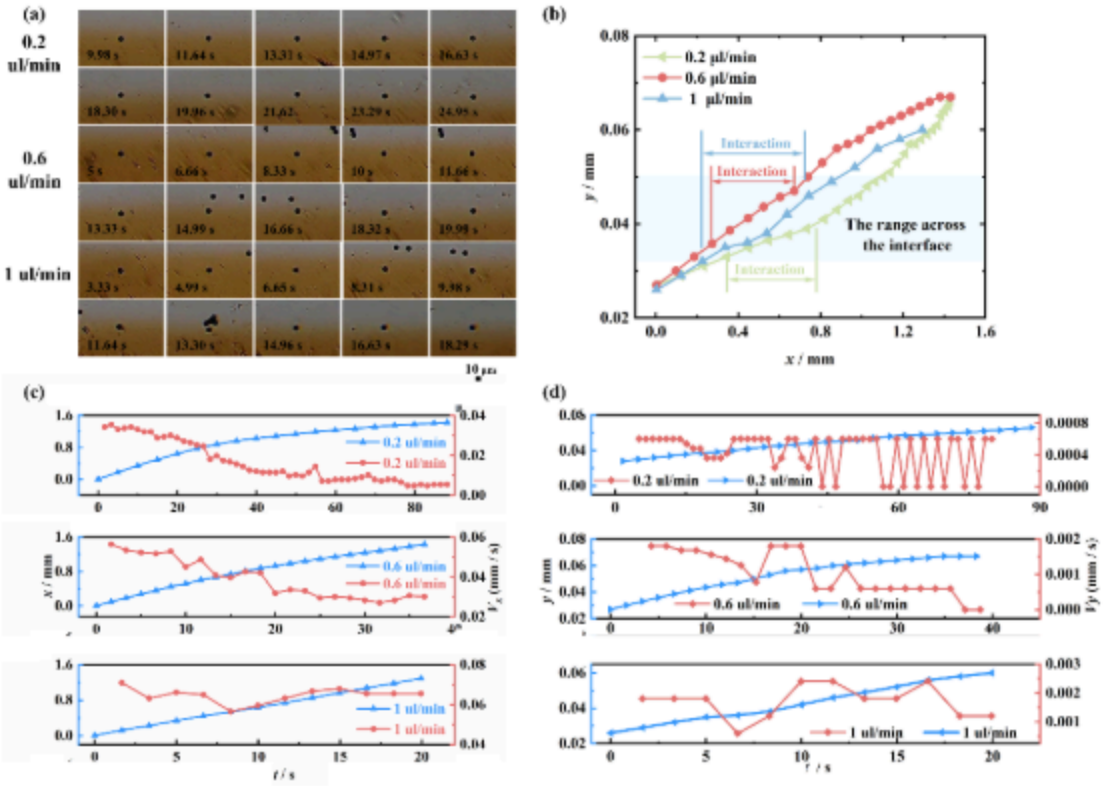


Figure 6

Experimental images, reconstructed particle trajectories, and time-resolved motion of 10 μm polystyrene particles at three volumetric flow rates (Qf = 0.2, 0.6, and 1.0 μL/min). (a) Sequential experimental micrographs (top to bottom: 0.2, 0.6, and 1.0 μL/min). (b) Reconstructed transverse position versus axial position, with the legend ordered 0.2, 0.6, and 1.0 μL/min. (c) Axial displacement (blue curves, left axis) and instantaneous axial velocity (red curves, right axis). (d) Transverse displacement (blue curves, left axis) and instantaneous transverse velocity (red curves, right axis). In (c) and (d), the stacked rows are arranged from top to bottom as 0.2, 0.6, and 1.0 μL/min; velocities are estimated from successive tracked positions.

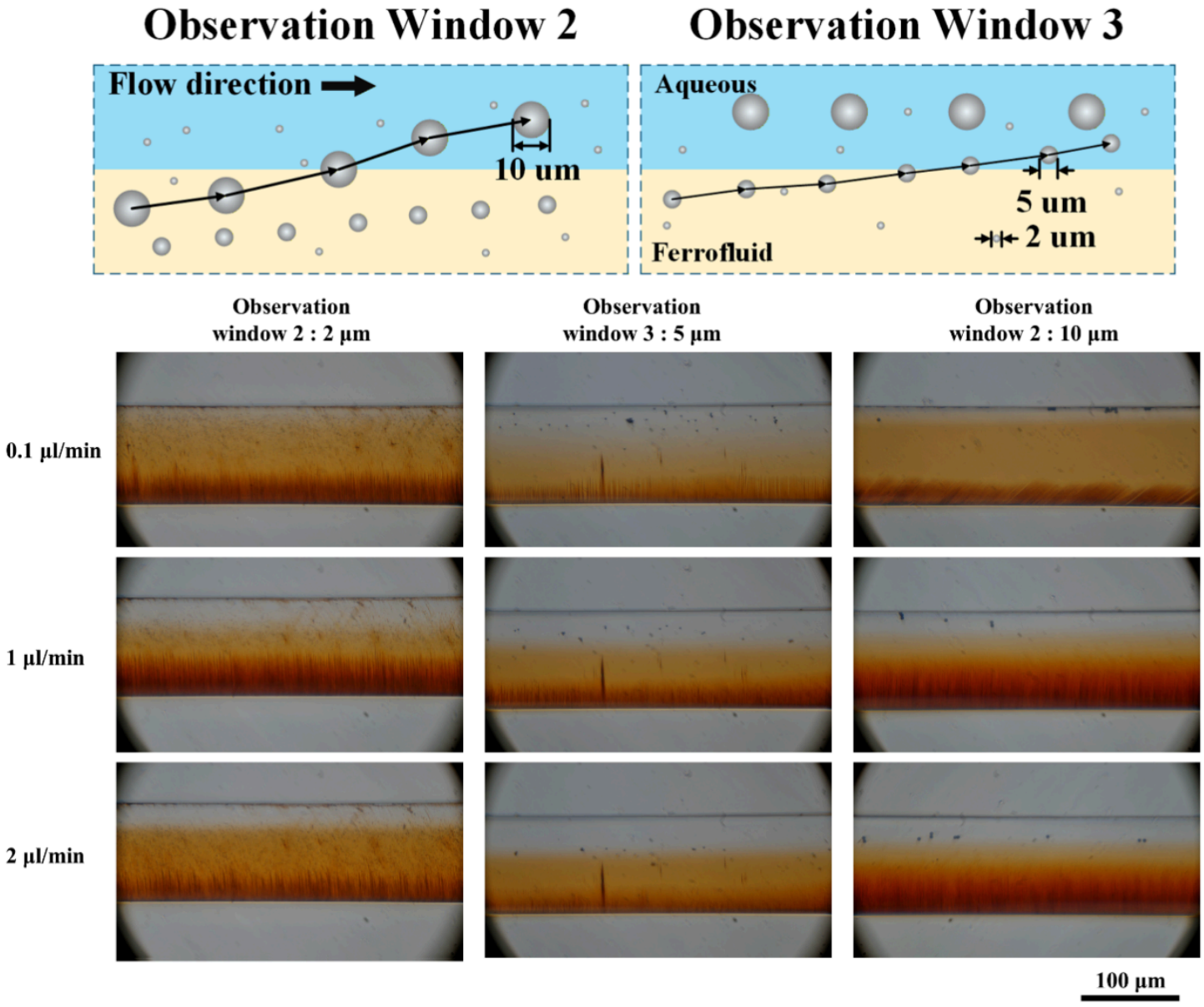


Figure 7

Schematic paths (top; not experimental tracks) and representative experimental micrographs (bottom).

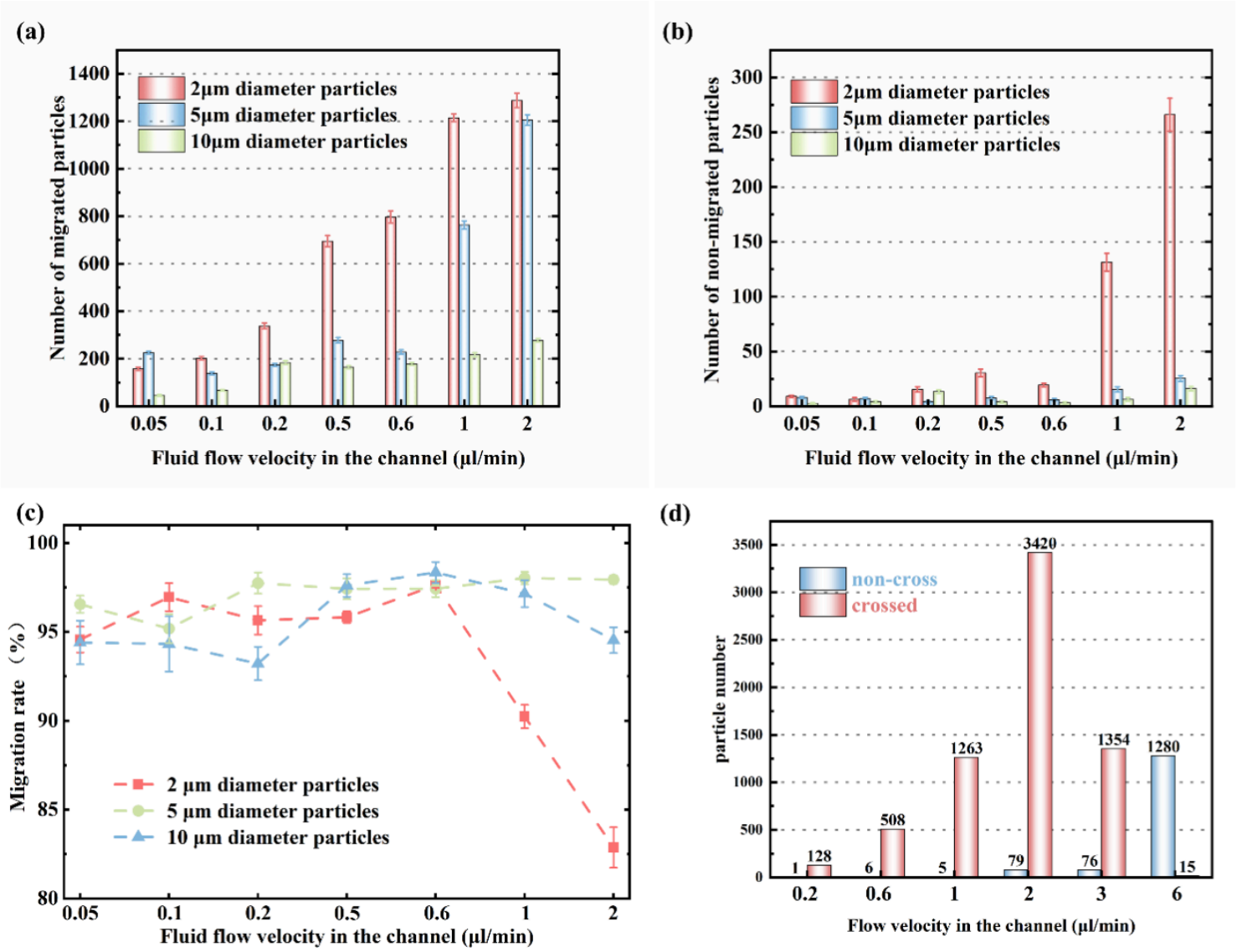


Figure 8

Particle counts and translocation efficiencies at different volumetric flow rates. (a) Counts of particles classified as translocated. (b) Counts of particles classified as non-translocated. (c) Translocation efficiency for 2 μm (red), 5 μm (green), and 10 μm (blue) particles, calculated from the counts in (a) and (b) as 100 × Ncross/(Ncross + Nnoncross). (d) Translocated and non-translocated counts for 10 μm particles over a separate, extended flow-rate range. The x-axis values are volumetric flow rates (μL/min), not linear velocities.

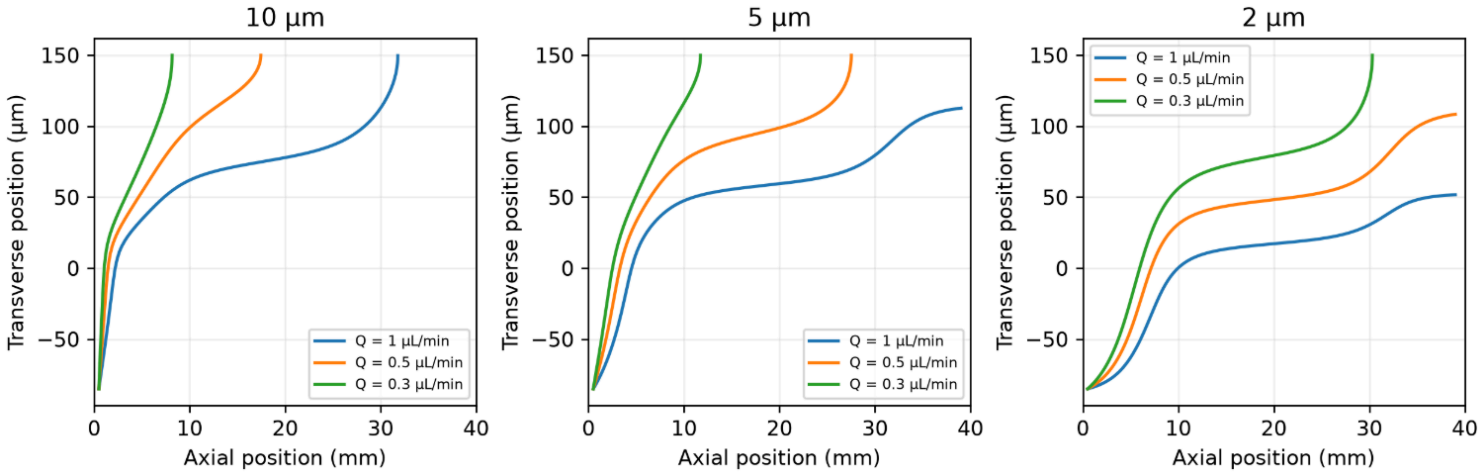


Figure 9

Simulated two-dimensional particle trajectories for d_p = 10, 5, and 2 µm at three per-inlet flow rates. Each panel represents one particle size; the colored curves terminate at x = 39 mm or at the model upper-wall limit. These are geometrical trajectories, and y = 0 does not represent a measured concentration boundary.

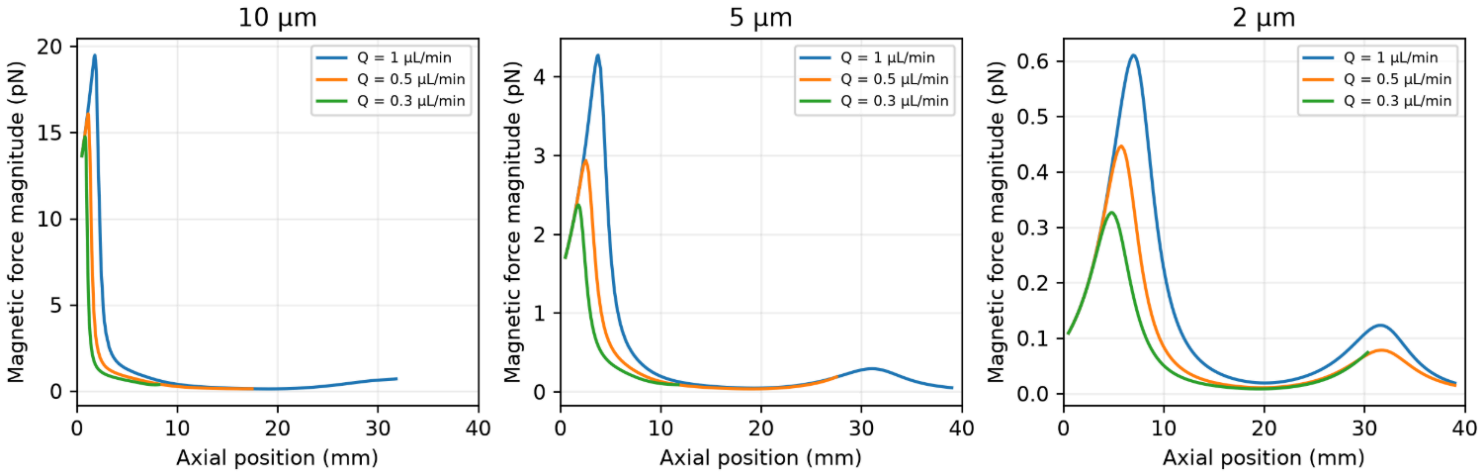


Figure 10

Magnitude of the prescribed magnetic force along the nine simulated trajectories. The force depends on the reference magnetic-force distribution, the interpolated normalized concentration, and the d_p^3 size-scaling factor.

Supplementary Files

This is a list of supplementary files associated with this preprint. Click to download.

- file.docx